submitted to *Biophys. J.* August-12, 2008
revised version: October-31, 2008

SUPPLEMENTARY MATERIAL:

# Structure of functional *Staphylococcus aureus* α-hemolysin channels in tethered bilayer lipid membranes

Duncan J. McGillivray,[1,2,§,‡] Gintaras Valincius,[3,‡] Frank Heinrich,[1,2] Joseph W. F. Robertson,[4] David J. Vanderah,[5] Wilma Febo-Ayala,[5,§§] Ilja Ignatjev,[3] Mathias Lösche[1,2,*] and John J. Kasianowicz[4]

1. National Institute of Standards and Technology (NIST) Center for Neutron Research (NCNR), Gaithersburg, Maryland 20899-6102
2. Physics Department, Carnegie Mellon University, Pittsburgh, Pennsylvania 15213-3890
3. Institute of Biochemistry, Mokslininku 12, LT-2600 Vilnius, Lithuania
4. Semiconductor Electronics Division, NIST, Electronics and Electrical Engineering Laboratory, Gaithersburg, Maryland 20899-8120
5. Biochemical Sciences Division, NIST, Chemical Sciences and Technology Laboratory, Gaithersburg, Maryland 20899-8313

This file describes the impedance spectroscopy data modeling and provides EIS results on αHL-reconstituted tBLMs in buffer (section I) and in PEG solutions (section II), and provides a full description of the neutron reflection data, models and scattering length density profiles (section III). It gives a determination of parameter confidence limits by a *Monte Carlo* resampling method (section IV) and describes auxiliary experiments with tBLMs using a longer tether (section V) that complement the results described in the main paper.

*Correspondence:

Mathias Lösche,
Physics Department, Carnegie Mellon University, 5000 Forbes Ave., Pittsburgh, PA 15213-3890
412-268-2735, fax: 412-268-8252, emb: quench@cmu.edu

## I. Modeling of electrochemical impedance spectra

To accurately determine area-normalized electronic components from EIS data, the roughness factor of each electrode was measured by two independent electrochemical techniques: capacitance ratio and gold oxide stripping coulometry (1) prior to the experiment, and determined as 1.39 ± 0.04. EIS data were fitted to the models in Scheme S1 using *Zview 2.9* (Scribner Associates, Inc., Southern Pines, NC), using data-modulus weighting. Model A, an equivalent circuit model (ECM) we recently developed, describes the properties of tBLMs particularly well (2-4). It accounts for the bilayer capacitance and the Helmholtz capacitance of an interface between the gold and the electrolyte ($CPE_{tBLM}$); a conduction pathway parallel to $CPE_{tBLM}$ consists of $CPE_{pores}$ and $R_{pores}$ and accounts for the conductance of either defects or αHL-induced pores. tBLM systems with a small defect density exhibit $CPE_{pores}$ exponent values close to α = 0.5, while an increasing density of the ion-conducting αHL pores shifts this parameter towards α = 1. $CPE_{pores}$ is determined by the Helmholtz capacitance and the specific conductance and thickness of the electrolyte reservoir confined between the electrode and the phospholipid bilayer. $R_{pores}$ corresponds to the resistance of the pores. Cole-Cole plots of electrochemical impedance spectra of an tBLM before and after αHL incubation, fitted to model A, are shown in Fig. S1.

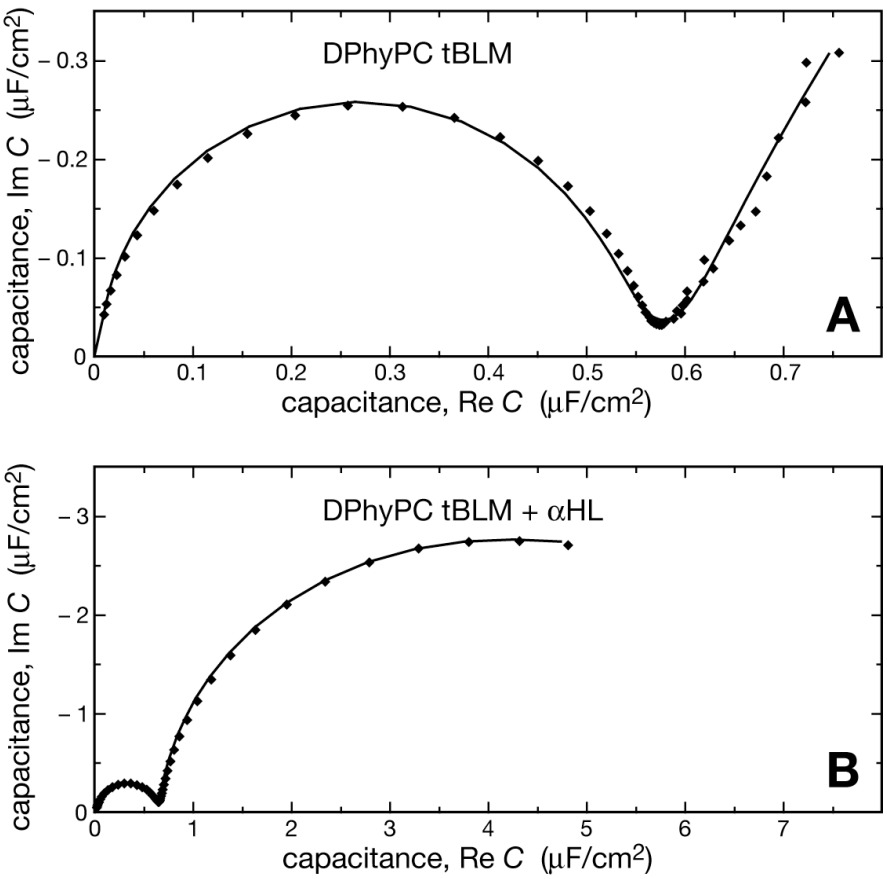


Figure S1: Cole-Cole plots of a DPhyPC tBLM before (A) and after (B) αHL reconstitution. (A) The tBLM was formed on a SAM prepared from a 30:70 (mol:mol) solution of WC14 and βME. The electrolyte was 0.1 M NaCl, 0.01 M Na-phosphate buffer at pH 7.5. Frequency range is from 1 to 65,000 Hz. (B) tBLM spectrum after incubation for 113 min with a 152 nM solution of αHL. Frequency range is from 1 to 39,800 Hz. All data are normalized with respect to the surface area. The solid lines show fits to ECM A of Scheme S1.

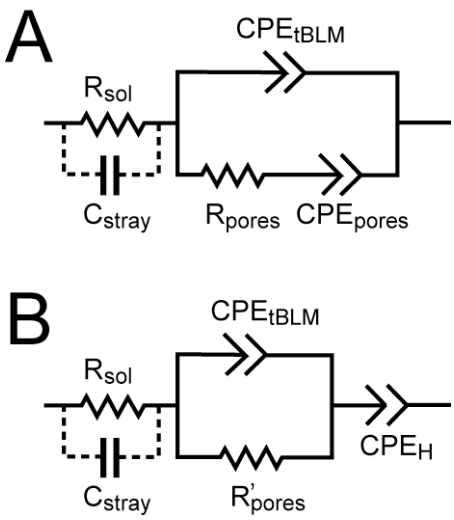


Scheme S1: Equivalent circuit models of the tBLM in solution. Two alternate models, A and B, were considered. The CPEs are constant phase elements, whose impedances are defined as $Z_{CPE} = 1/CPE \times 1/(i\omega)^{\alpha}$, where CPE is the coefficient of the element. $\omega = 2\pi f$, with $f$ the frequency in Hz. α is the CPE exponent. $R_{sol}$ is the solution resistance, and $C_{stray}$ accounts for the capacitance associated of cables, connectors and the electrochemical cell. Model A attributes a constant phase element $CPE_{pores}$ to the pores in the membrane whereas model B assumes a $CPE_H$ for the Helmholtz layer.

EI spectra fitted with ECM A yielded fit qualities of (typically) $\chi^2 < 2\times10^{-4}$. Results are summarized in Table S1. Incubation with αHL solution increases $CPE_{tBLM}$ as well as $CPE_{pores}$ and $\alpha_{pores}$. However, the most dramatic change occurs in $R_{pores}$, which exhibits a ca. 30-fold decrease upon incubation with protein solution, which we attribute to the αHL-induced conductance, $Y_{pores} = R_{pores}^{-1}$, of the membrane.

We considered other ECMs for the tethered membranes (***e.g.***, ECM B in Scheme S1). These did not fit the experimental data well compared to ECM A. Under certain conditions, the two models, A and B, may be degenerate, which may lead to a different interpretation of the electrochemical properties of the interface. Specifically, the exponent of $CPE_{pores}$ increased from $\alpha_{pores} \approx 0.5$ to $\alpha_{pores} \rightarrow \alpha_{tBLM}$ upon incubation with αHL (see Table S1). At $\alpha_{pores} = \alpha_{tBLM}$, model A becomes degenerate with model B. Upon incubation with αHL, the exponent of $CPE_{pores}$ increased from $\alpha_{pores} \approx 0.5$ to $\alpha_{pores} \rightarrow \alpha_{tBLM} \approx 0.98$ (Table S1). In the degenerate case, the pore conductance described as $R_{pores}$ in series with $CPE_{pores}$ parallel to the insulating membrane is replaced by (5)

$$R'_{pores} = R_{pores} \cdot \left( \frac{CPE_{pores}}{CPE_{pores} + CPE_{tBLM}} \right)^2 \qquad (1)$$

Because $R'_{pores} < R_{pores}$, the αHL-induced conductance across the membrane is greater in ECM B than in ECM A. Although $\alpha_{pores}$ is not strictly equal to $\alpha_{tBLM}$, the uncertainty in α limits our ability to distinguish between the two models. A best-fit parameter set is included in Table S1 for comparison with the best fit using ECM A. In this case, $\chi^2$ must be tested for both models. Indeed, the $\chi^2$ for model A is about 10-fold smaller than that for model B. Moreover, while $R_{pores}$ is less in model B than in model A, it is also significantly less than predicted by Eqn. (1), which is physically unrealistic. This rules out the possibility of degeneracy and justifies the validity of model A.

Table S1: Model parameters for the DPhyPC tBLM EIS spectra shown in Fig. S1 derived from a single sample. Data is normalized with respect to the real surface area. Normalization of $R_{sol}$ and $C_{stray}$ keeps the whole data set consistent.

| parameter \ system | tBLM before αHL reconstitution (model A) | tBLM after αHL reconstitution (model A) | tBLM after αHL reconstitution (model B) |
|---|---|---|---|
| $CPE_{tBLM}$, $\mu F \cdot cm^{-2} \times s^{(\alpha-1)}$ | 0.696 ± 0.007 | 0.791 ± 0.003 | 0.908 ± 0.016 |
| $\alpha_{tBLM}$ | 0.975 ± 0.001 | 0.9741 ± 0.0004 | 0.992 ± 0.004 |
| $CPE_{pores}$, $\mu F \cdot cm^{-2} \times s^{(\alpha-1)}$ | 1.575 ± 0.119 | 7.38 ± 0.04 | |
| $\alpha_{pores}$ | 0.51 ± 0.10 | 0.86 ± 0.04 | |
| $CPE_{H}$, $\mu F \cdot cm^{-2} \times s^{(\alpha-1)}$ | | | 7.87 ± 0.12 |
| $\alpha_{H}$ | | | 0.87 ± 0.01 |
| $R_{pores}$, $k\Omega \cdot cm^2$ | 305 ± 15 | 12.25 ± 0.04 | 8.80 ± 0.15 |
| $R_{sol}$, $\Omega \cdot cm^2$ | 53.8 ± 0.2 | 65.4 ± 0.1 | 64.3 ± 0.3 |
| $C_{stray}$, $nF \cdot cm^{-2}$ | 6.14 ± 0.35 | 7.99 ± 0.16 | 7.06 ± 0.51 |
| $\chi^2$ | $15.1 \cdot 10^{-5}$ | $1.52 \cdot 10^{-5}$ | $14.6 \cdot 10^{-5}$ |

**II. EIS of protein-reconstituted tBLMs in PEG solutions**

Upon introduction of differently-sized PEGs (15% w/w), reversible changes in the EIS data were observed in the frequency range that is mostly determined by $R_{pores}$, as the modeling shows. In particular PEGs with a mean molecular mass < 2,250 g/mol increased $|Z|$ and shifted the minimum in $\phi$ towards lower frequencies (Fig. S2), while PEGs with a mean molecular mass > 2,250 g/mol caused the opposite effects. Representative fits to the model obtained on one single tBLM are listed in Table S2. The PEGs affect mainly $R_{pores}$, which changes by ≈ –35% (PEG200) to ≈ +15% (PEG3400) from its value in PEG-free buffer. Other parameters were less affected by the polymer, except for $CPE_{pores}$, which changed by –10% in PEG200, presumably due to penetration of polymer molecules into the submembrane space.

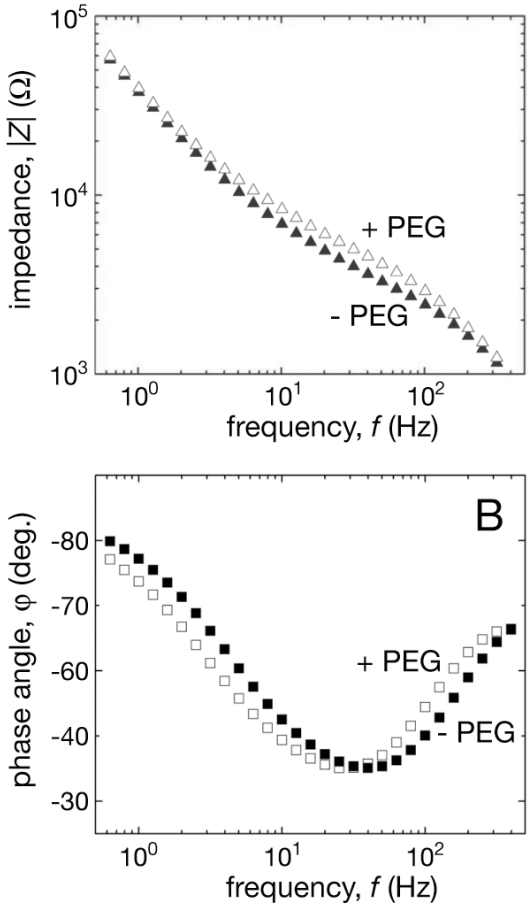


Figure S2: Effect of 15% (w:w) 400 g/mol PEG on the impedance (Bode plots) of a tBLM containing αHL channels. Data are normalized with respect to the surface area.

Table S2: Model parameters for tBLMs in solutions without and with differently-sized PEG.[a,b,c]

| parameter | no PEG | 15% w/w PEG200 (relative changes) | 15% w/w PEG3400 (relative changes) |
|---|---|---|---|
| $CPE_{tBLM}$, μF · cm$^{-2}$×s$^{(α-1)}$ | 0.793 | 0.818 (+3%) | 0.862 (+8%) |
| $α_{tBLM}$ | 0.974 | 0.969 (–1%) | 0.963 (–1%) |
| $CPE_{pores}$, μF · cm$^{-2}$×s$^{(α-1)}$ | 4.04 | 3.64 (–10%) | 4.11 (+2%) |
| $α_{pores}$ | 0.844 | 0.856 (+1%) | 0.846 (+0%) |
| $Y_{pores} = R_{pores}^{-1}$, μS · cm$^{-2}$ | 638 | 414 (–35%) | 717 (+12%) |
| $χ^2$ | $8.1 \cdot 10^{-5}$ | $9.3 \cdot 10^{-5}$ | $8.2 \cdot 10^{-5}$ |

[a]The buffer was 0.1 M NaCl, 0.01 M Na-phosphate at pH 7.5.
[b]The tBLM was incubated for ca. 1 h with 50 nM αHL solution in a similar buffer at pH 4.5. The incubation solution was then replaced with buffer (pH 7.5) that was free of αHL.
[c]Numbers in parentheses indicate changes of a particular parameter with respect to its value in a PEG-free solution. Relative fitting errors were below 1% for all listed parameters.

## III. Neutron reflection

*αHL reconstituted into WC14-based tBLMs.* Figure S3 shows the full range of experiments with isotopically distinct bulk solvents performed before and after the incorporation of αHL into the membrane. Addition of αHL into the membrane resulted in subtle, yet significant changes in the NR spectra, particularly at low momentum transfer $Q_z$.

These data were fitted using a slab model with layers of uniform neutron scattering length density (nSLD) for each of the chemically distinct components of the interface: Si, $SiO_x$, Cr, Au, OEG tether, inner bilayer leaflet, outer bilayer leaflet, headgroups, and solvent. In the composition-space refinement evaluation (6,7) of the neutron reflection data, nSLDs in slabs representing the tBLM and αHL ($z$ = 0 – 120 Å in Fig. S4) was parameterized in terms of volume fractions, η, of organic material and solvent (8), subject to the constraint $\sum \eta_j = 1$, i.e. volume not occupied by organic material is filled by aqueous buffer of the appropriate isotopic composition. For example, the hydration of a lipid headgroup (hg) layer is the composite result of three NR spectra measured with different neutron contrasts:

$$\eta_{water} = \frac{n_w \cdot V_w}{n_w \cdot V_w + V_{hg}} = \frac{V_w\left(\rho^w V_{hg} - b_{hg}\right)}{V_w\left(\rho^w V_{hg} - b_{hg}\right) - V_{hg}\left(\rho^w V_w - b_w\right)} \qquad (2)$$

where $n_w$ is the (fractional) number of waters per lipid hg, $V$ is a molecular volume [$V_w$ = 10 Å$^3$ for water, indiscriminate of isotopic composition, $V_{hg}$ = 200 Å$^3$, see (9)] and $b$ is neutron scattering length. The subscript $w$ (= $D_2O$, CM4, $H_2O$) indicates the isotopic composition of water and ρ is the experimentally determined nSLD, measured in the system under three distinct isotopic buffer compositions specified by the superscript. Similar relations hold for the alkane region, where the monolayer proximal to the solid support is frequently slightly incomplete and incorporates water-filled defects amounting to typically 5% of its overall area.

It has been determined from grazing-incidence x-ray diffraction studies of a large number of amphiphiles in Langmuir monolayers (10) that the alkane density in lipid membranes cannot exceed 1 alkane chain per 19.5 Å$^2$. For the evaluation of NR data, this confines the nSLD of the alkane phase to be $\rho > -0.5\times10^{-6}$ Å$^{-2}$. While restricting the phytyl nSLD to fall above this lower limit in the model, we observed that the best-fit parameters in histograms derived from a novel Monte-Carlo resampling procedure (details, see section IV.) for $\rho_{phytyl}$ peaked at this limit. Consequently, we denoted this parameter as “fixed” at this value (Table S3). This best-fit model suggests an unphysically high phytyl chain density. However, the deviation of this result from the expected value, $\rho_{phytyl} \approx -0.3\times10^{-6}$ Å$^{-2}$ (11,12), equals the typical measurement uncertainty of this parameter. In fact, we occasionally observed a similar overestimation of non-deuterated al-

kane chain density for various non-deuterated lipids when using box models for data analysis. We assume that this is due to intrinsic weaknesses of the box model in describing the interface between phospholipid headgroups and alkyl chains, studied extensively in earlier work on Langmuir monolayers (13). While we were able to resolve this flaw of the box model in developing more complex phospholipid models for Langmuir monolayers (14), we note that the application of an adequately complex model for bilayer lipids is currently beyond the scope of or modeling capabilities of tBLMs, and may exceed the information content of the obtained reflectivity data. We thoroughly verified that variations in the model using fixed values for $\rho_{phytyl}$ between –0.5 and $–0.3\times10^{-6}$ $Å^{-2}$ did not significantly alter the structural impact of αHL incorporation on the bilayer and are therefore confident that our conclusions in the paper are not affected by this result.

The αHL spans several layers in the model; the contribution of the protein to the nSLD of these layers was calculated from the published crystal structure (15). For convenience in the model evaluation, the in-plane protein density $\sigma_{αHL}$ in/at the membrane was parameterized in terms of a square lattice of protein caps in the layer adjacent to the tBLM, assuming that the diameter of the cap sets the limit for dense packing. The evaluation of this parameter is reported in Fig. S5A (green plot symbols). In distinction, the protein density reported in Table S3 was converted assuming a hexagonal lattice parameter according to the relation:

$$\sigma_{\alpha HL}^{hex} = \sqrt{3}/2 \times \sigma_{\alpha HL}^{square}.$$

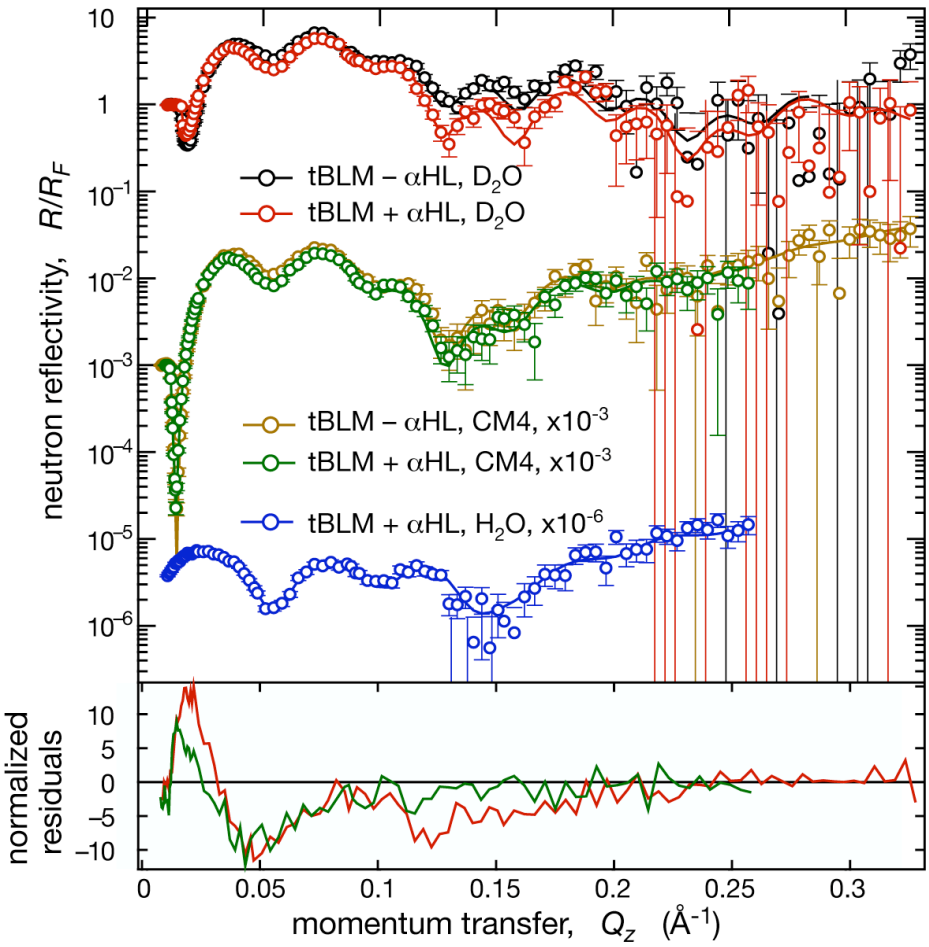


Figure S3: Comprehensive NR data. Main panel: Fresnel-normalized NR reflection data sets obtained from one tBLM (WC14:βME = 30:70, completed with DPhyPC) before and after reconstitution of αHL channel proteins at various solvent contrasts. The upper pair of data sets are identical with those in Fig. 3 in the paper. Lower panel: Error-weighted residuals between data with αHL and without αHL. The red line ($D_2O$ data sets) is the same as in Fig. 3. The green line is for the CM4 data sets. Solid lines in the main panel are the reflectivities computed from the nSLD profiles shown in Fig. S4.

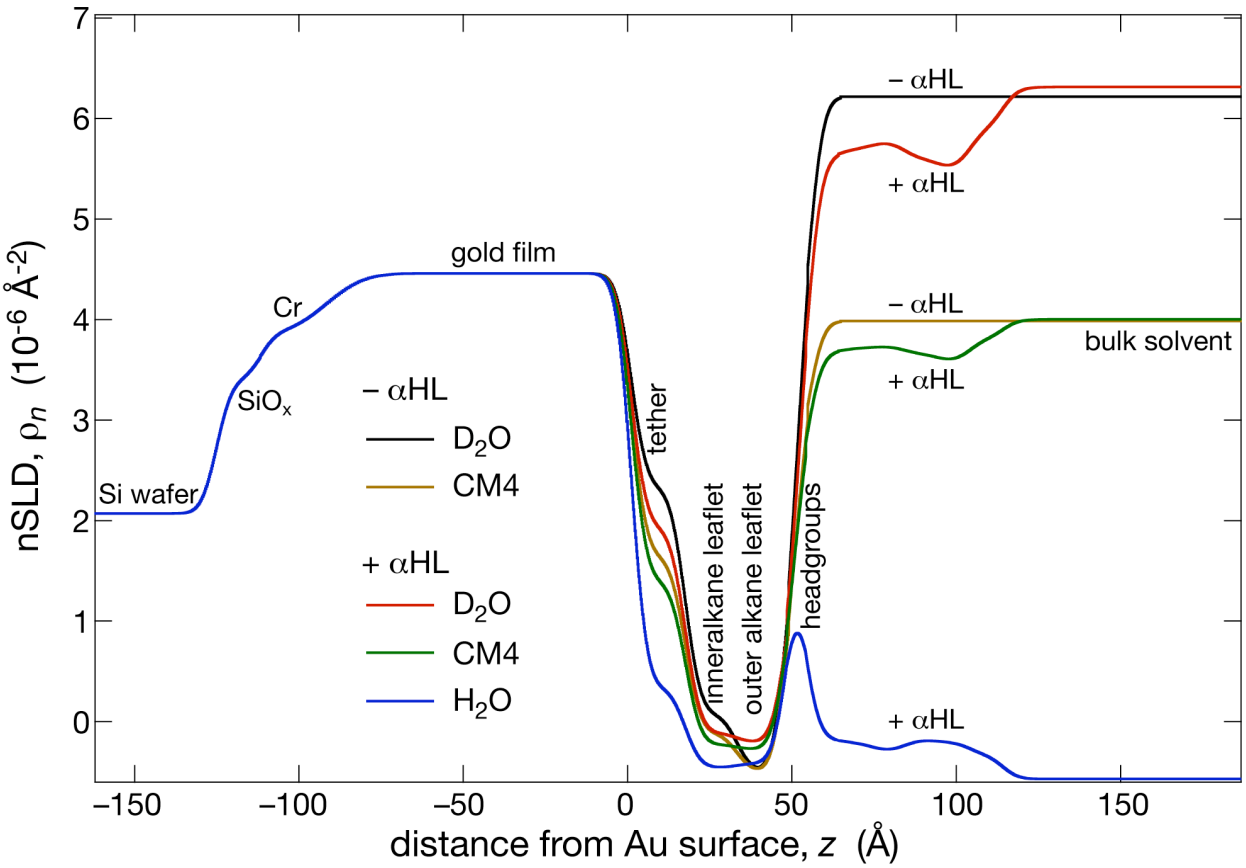


Figure S4: Neutron scattering length density profiles derived from a simultaneous model fit to all data shown in Fig. S3. The color code is consistent with that of the data sets. Details are presented in Table S3.

Table S3: Model parameters derived from a simultaneous fit to NR data at different solvent contrasts for a tBLM prepared with WC14/βME (1:3) and DPhyPC, with and without αHL.[a,b]

| parameter \ data set | – αHL, $D_2O$ buffer | – αHL, CM4 | + αHL, $D_2O$ buffer | + αHL, CM4 | + αHL, $H_2O$ buffer |
|---|---|---|---|---|---|
| thickness $SiO_x$, Å | 16.1 ± 0.9 | | | | |
| thickness Cr, Å | 22.4 ± 1.0 | | | | |
| thickness Au, Å | 88.0 ± 1.0 | | | | |
| thickness tether layer, Å | 17.0 ± 0.7 | | | | |
| thickness inner/outer alkane layer[c], Å | 15.4 ± 0.4 | | 14.9 ± 0.4 | | |
| thickness outer headgroup layer, Å | 7.6 ± 0.4 | | 7.8 ± 0.4 | | |
| penetration depth of αHL[d], Å | n/a | | –42.8 ± 1.1 | | |
| lipid nSLD, $10^{-6}$ Å$^{-2}$ | –0.50 (fixed) | | | | |
| nSLD bulk solvent, $10^{-6}$ Å$^{-2}$ | 6.22 ± 0.01 | 3.99 ± 0.01 | 6.31 ± 0.01 | 4.00 ± 0.01 | –0.56 (fixed) |
| vol. fraction of water in tether layer | 0.29 ± 0.02 | | 0.21 ± 0.02 | | |
| vol. fraction of water in inner lipid leaflet[e] | 0.08 ± 0.01 | | 0.04 ± 0.01 | | |
| vol. fraction of water in outer lipid leaflet[e] | 0.00 ± 0.01 | | 0.00 ± 0.01 | | |
| vol. fraction of water in outer headgroup layer[e] | 0.45 ± 0.09 | | 0.13 ± 0.08 | | |
| in-plane αHL density[f] | n/a | | 33 ± 1% | | |
| global roughness, Å | 6.9 ± 1.0 | | | | |
| $\chi^2$ | 2.13 | 2.52 | 3.45 | 1.79 | 1.14 |
| $\chi^2$ (global) | 2.37 | | | | |

[a]Parameter values printed across neighboring columns were determined by requiring that those parameters fit the data sets represented in these columns simultaneously (6,7).
[b]nSLDs were taken from tabulated values or estimated from molecular models: Si ($2.07\times10^{-6}$ Å$^{-2}$), $SiO_x$ ($3.4\times10^{-6}$ Å$^{-2}$), Au ($4.5\times10^{-6}$ Å$^{-2}$), $HS(EO)_6$-glycerol tethers, βME and phosphatidylcholine headgroups within the tether layer ($0.60\times10^{-6}$ Å$^{-2}$), outer phosphatidylcholine headgroup layer ($1.8\times10^{-6}$ Å$^{-2}$).
[c]The inner and outer alkane layers were assumed to be of equal thickness.
[d]"Penetration depth of αHL" refers to the difference between the upper interface of the outer lipid headgroup layer and the lower end of the αHL stem.
[e]The remaining content of these layers is composed of lipid and protein material in a composition that derives from the amino acid composition along the protein's symmetry axis, as determined from the αHL crystal structure (15), the in-plane density of αHL and the protein's penetration depth into the bilayer.
[f]"In-plane αHL density" refers to a dense hexagonal packing of the protein caps in the layer outside of the tBLM, assuming a cap diameter, $D_{cap}$ = 105 Å.

## IV. Determination of parameter confidence limits in neutron reflection

Because the interference patterns of the NR results are dominated by the physical properties of the inorganic surface structure of the support (primarily, the gold film), it is important to show that all parameters are well determined in the composition-space refinement procedure. Thus, we determined the confidence limits of the model by *Monte Carlo* resampling of synthetic data sets (16).

In this procedure, $N$ = 1,000 synthetic data sets were cloned from the experimental data by creating random, Gaussian-weighted deviations from the true data based on the uncertainty of each experimental data point determined by counting statistics. By coupling these simulated data sets in the same way as in the determination of the best-fit model (indicated by parameter spreading across the columns in Table S3), $N$ slightly different best-fit parameter sets were determined. The best-fit parameter sets were binned and analyzed. In most cases, the resulting parameter distributions were well described by Gaussians. Because some distributions showed asymmetric tails, uncertainties are reported as (standard deviation $\sigma \times \sqrt{2}$), representing ca. 84% confidence limits.

Further to providing an objective measure of the parameter confidence limits, *Monte Carlo* resampling shows that the model is adequately parameterized given the quality of the experimental data, because it resulted in narrow histograms that were in most cases Gauss-shaped. If the model were overparameterized, one would expect flat histogram distributions that are not seen in the results. The *Monte Carlo* resampling also provides evidence that we obtain the global minimum within our model. If the fit were trapped in local minima, this would have produced parameter distributions with multiple peaks. However, that was not the case (see Fig. S5).

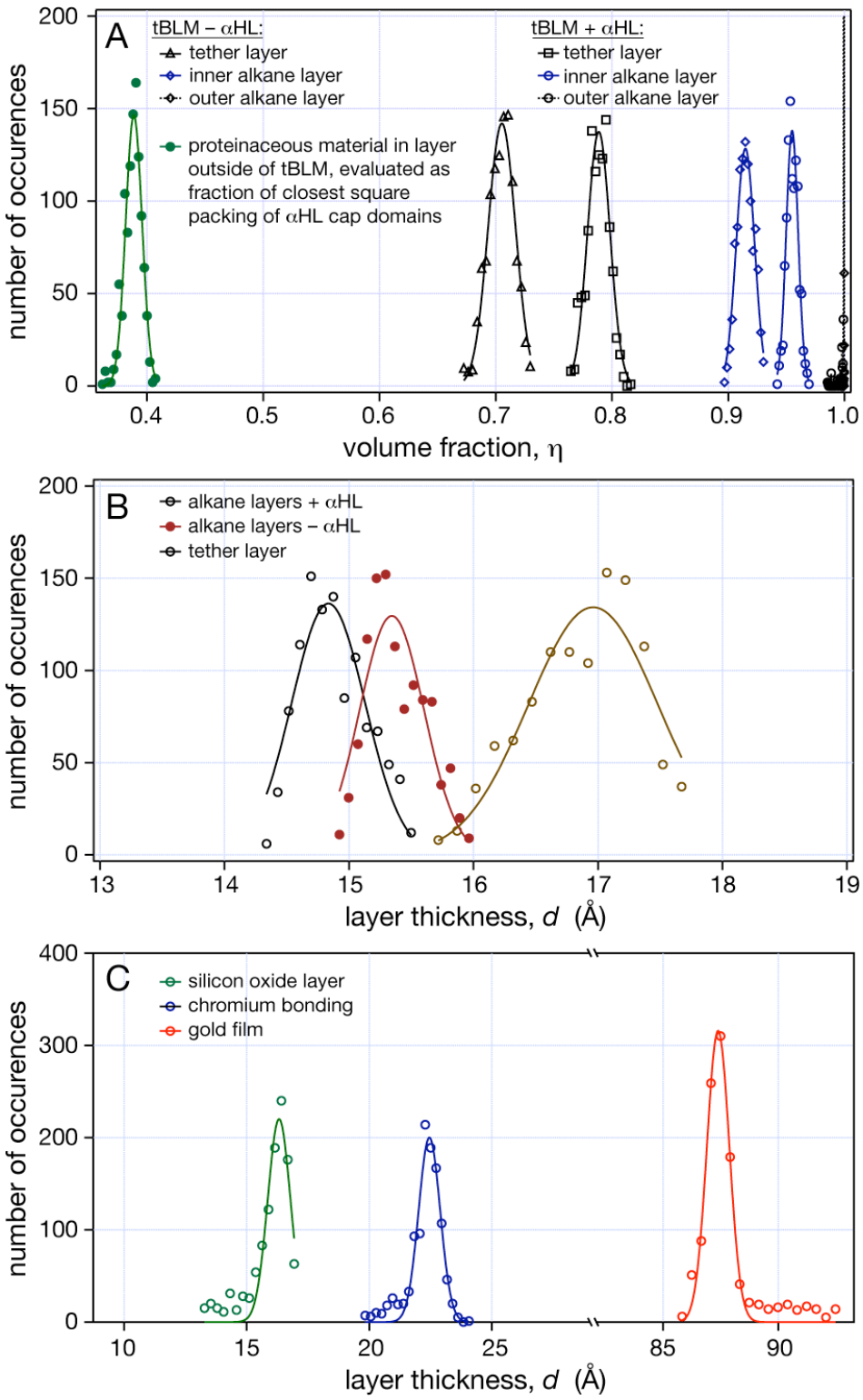


Figure S5: Results from *Monte Carlo* resampling. Parameter distribution histograms for (A) volume fraction of the organic materials, (B) geometric properties of the layers that compose the tBLM and (C) geometric properties of the inorganic substrate surface structure. Continuous lines are Gaussian fits.

## V. Bilayers from PDP-PEG2000-DSPE-based bilayer surfaces

To test the effect of the proximity of the gold surface on the structural details of αHL membrane incorporation, control experiments were performed with PDP-PEG2000-DSPE-based tBLMs. Fig. S6 shows a complete solvent contrast data set collected for such a surface. Modeling was performed using the same conditions as for WC14-based tBLMs. The result in Fig. S7 shows that the PEG moiety ($n \approx 45$) increases the thickness of the space between the gold electrode and the inner membrane leaflet to ≈ 60 Å. Although these tBLMs are not electrically insulating, NR shows that the membrane covers the gold surface homogeneously and that αHL reconstitution occurs as it does in the WC14-based tBLMs. *Monte Carlo* resampling of the results in Fig. S6 suggests that the differences between the neutron reflectivities in the absence and presence of αHL are statistically significant (*not shown*). The nSLD profiles (Fig. S7) suggest that protein association with the membrane is similar in both systems. Thus, the structural organization of the reconstituted protein in the membrane does not depend on distance from the gold electrode.

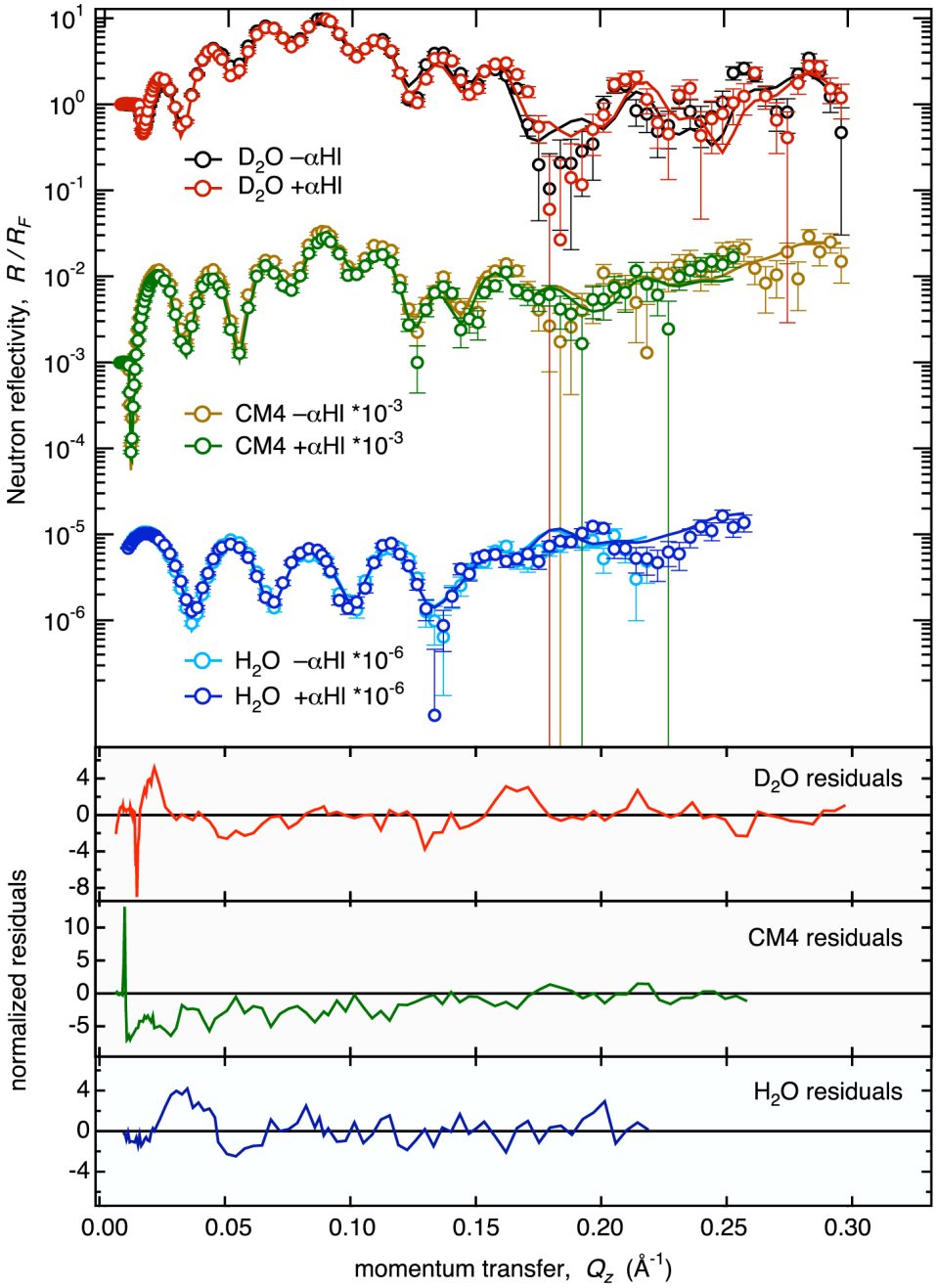


Figure S6: NR data for an alternate tBLM preparation. Main panel: Fresnel-normalized NR reflection data sets obtained from a tBLM (PDP-PEG2000-DSPE, completed with DPhyPC) before and after reconstitution of αHL channel proteins at various solvent contrasts. Lower panel: Error-weighted residuals between data with αHL and without αHL. Solid lines in the main panel are the reflectivities computed from the nSLD profiles shown in Fig. S7.

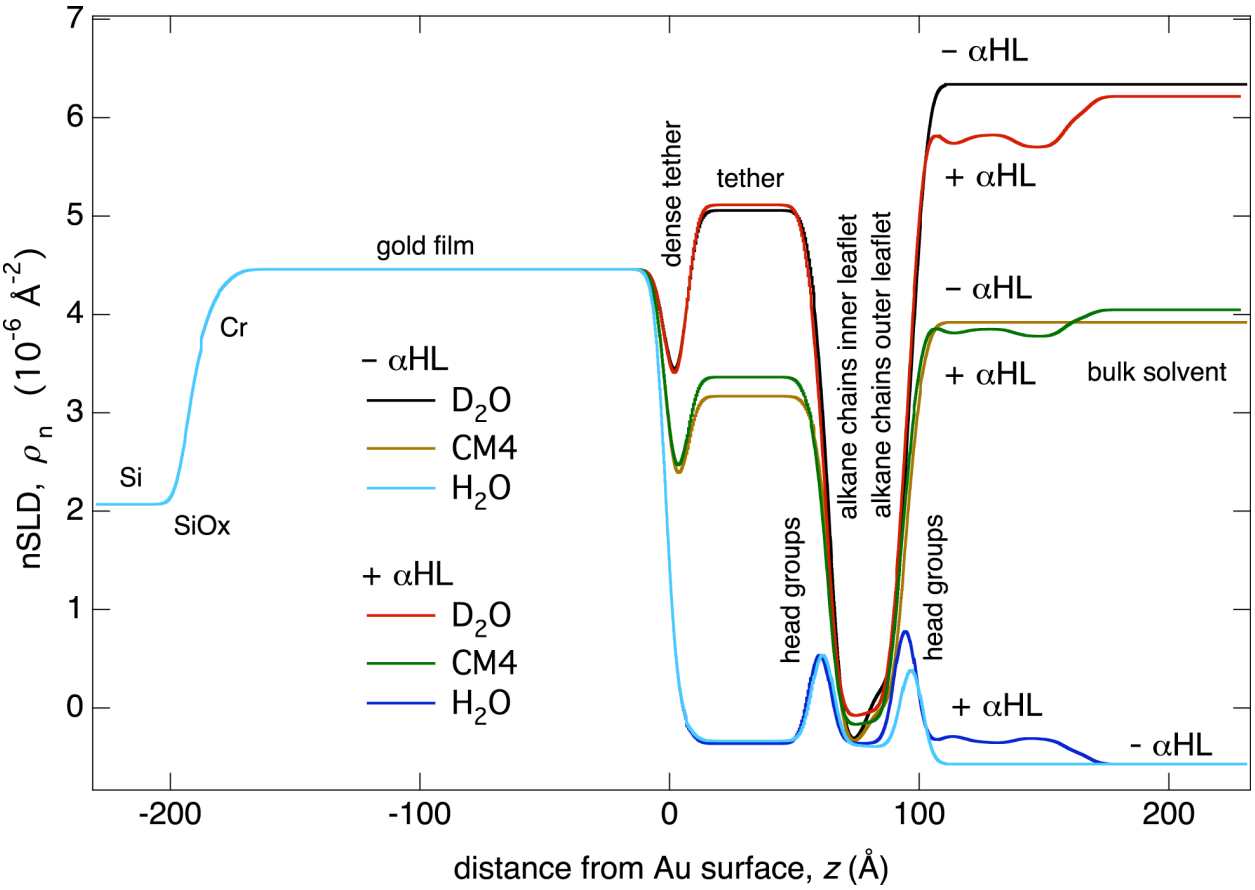


Figure S7: nSLD profiles derived from a simultaneous model fit to all data sets shown in Fig. S6. The color code is consistent with that of the data sets. Details are presented in Table S4.

Table S4: Model parameters derived from a simultaneous fit to NR data at different solvent contrasts for a tBLM prepared with PDP-PEG2000-DSPE and DPhyPC, without and with αHL.[a,b]

| parameter \ data set | – αHL, $D_2O$ buff. | – αHL, CM4 | – αHL, $H_2O$ buff. | + αHL, $D_2O$ buff. | + αHL, CM4 | + αHL, $H_2O$ buff. |
|---|---|---|---|---|---|---|
| thickness $SiO_x$, Å | 6.7 ± 5.5 | | | | | |
| thickness Cr, Å | 7.2 ± 5.9 | | | | | |
| thickness Au, Å | 178.6 ± 2.4 | | | | | |
| thickness dense tether layer, Å | 8.5 ± 0.8 | | | | | |
| thickness highly hydrated tether layer, Å | 51.3 ± 0.9 | | | 49.9 ± 0.9 | | |
| thickness inner/outer alkane layer, Å | 14.3 ± 0.5 | | | 13.7 ± 0.5 | | |
| thickness headgroup layers, Å | 7.0 (fixed) | | | | | |
| penetration depth of αHL, Å | n/a | | | –35.8 ± 9.0 | | |
| lipid nSLD, $10^{-6}$ Å$^{-2}$ | –0.40 (fixed) | | | | | |
| nSLD bulk solvent, $10^{-6}$ Å$^{-2}$ | 6.21 ± 0.01 | 4.05 ± 0.01 | –0.56 (fixed) | 6.33 ± 0.01 | 3.92 ± 0.01 | –0.56 (fixed) |
| vol. fraction of water in dense tether layer | 0.44 ± 0.04 | | | | | |
| vol. fraction of water in hydrated tether layer | 0.78 ± 0.01 | | | 0.80 ± 0.01 | | |
| vol. fraction of water in inner headgroup layer | 0.33 ± 0.08 | | | | | |
| vol. fraction of water in inner lipid leaflet | 0.00 ± 0.03 | | | 0.02 ± 0.03 | | |
| vol. fraction of water in outer lipid leaflet | 0.09 ± 0.03 | | | 0.04 ± 0.03 | | |
| vol. fraction of water in outer headgroup layer | 0.41 ± 0.10 | | | 0.17 ± 0.09 | | |
| in-plane αHL density | n/a | | | 24 ± 2% | | |
| global roughness, Å | 8.6 ± 0.6 | | | | | |
| $\chi^2$ | 4.06 | 4.31 | 3.69 | 4.84 | 5.01 | 3.79 |
| $\chi^2$ (global) | 4.55 | | | | | |

[a]Parameter values printed across neighboring columns were determined by requiring that those parameters fit the data sets represented in these columns simultaneously.
[b]Uncertainties were determined from the covariance matrix of a Levenberg-Marquardt least square minimization.

## REFERENCES


1. Trasatti, S. and O. A. Petrii. 1991. Real surface area measurements in electrochemistry. *Pure Appl. Chem.* 63:711-734.
2. McGillivray, D. J., G. Valincius, D. J. Vanderah, W. Febo-Ayala, J. T. Woodward, F. Heinrich, J. J. Kasianowicz, and M. Lösche. 2007. Molecular-scale structural and functional characterization of sparsely tethered bilayer lipid membranes. *Biointerphases* 2:21-33.
3. Valincius, G., F. Heinrich, R. Budvytyte, D. J. Vanderah, Y. Sokolov, J. E. Hall, and M. Lösche. 2008. Soluble amyloid oligomers affect dielectric membrane properties by bilayer insertion and domain formation: Implications for cell toxicity. *Biophys. J.* 95:4845-4861.
4. Valincius, G., D. J. McGillivray, W. Febo-Ayala, D. J. Vanderah, J. J. Kasianowicz, and M. Lösche. 2006. Enzyme activity to augment the characterization of tethered bilayer membranes. *J. Phys. Chem. B* 110:10213-10216.
5. Berthier, F., J. P. Diard, and R. Michel. 2001. Distinguishability of equivalent circuits containing CPEs: Part I. Theoretical part. *J. Electroanal. Chem.* 510:1-11.
6. Vaknin, D., K. Kjaer, J. Als-Nielsen, and M. Lösche. 1991. Structural properties of phosphatidylcholine in a monolayer at the air/water interface. Neutron reflection study and reexamination of x-ray reflection experiments. *Biophys. J.* 59:1325-1332.
7. Wiener, M. C. and S. H. White. 1991. Fluid bilayer structure determination by the combined use of x-ray and neutron diffraction. II. "Composition-space" refinement method. *Biophys. J.* 59:174-185.
8. Schalke, M., P. Krüger, M. Weygand, and M. Lösche. 2000. Submolecular organization of DMPA in surface monolayers: Beyond the two-layer model. *Biochim. Biophys. Acta* 1464:113-126.
9. Armen, R. S., O. D. Uitto, and S. E. Feller. 1998. Phospholipid component volumes: Determination and application to bilayer structure calculations. *Biophys. J.* 75:734-744.
10. Kaganer, V. M., H. Möhwald, and P. Dutta. 1999. Structure and phase transitions in Langmuir monolayers. *Rev. Mod. Phys.* 71:779-819.
11. Wu, Y., K. He, S. J. Ludtke, H. W. Huang. 1995. X-ray diffraction study of lipid bilayer membranes interacting with amphiphilic helical peptides: diphytanoyl phosphatidylcholine with alamethicin at low concentrations. *Biophys. J.* 68:2361-2369.
12. Husslein, T., D. M. Newns, P. C. Pattnaik, Q. Zhong, P. B. Moore, and M. L. Klein. 1998. Constant pressure and temperature molecular-dynamics simulation of the hydrated diphytanolphosphatidylcholine lipid bilayer. *J. Chem. Phys.* 109: 2826-2832.
13. Schalke, M. and M. Lösche. 2000. Structural models of lipid surface monolayers from X-ray and neutron reflectivity measurements. *Adv. Colloid Interf.* 88:243-274.
14. Schalke, M., P. Krüger, M. Weygand, and M. Lösche. 2000. Submolecular organization of DMPA in surface monolayers: Beyond the two-layer model. *Biochim. Biophys. Acta* 1464:113-126.
15. Song, L., M. R. Hobaugh, C. Shustak, S. Cheley, H. Bayley, and J. E. Gouaux. 1996. Structure of staphylococcal α-hemolysin, a heptameric transmembrane pore. *Science* 274:1859-1865.
16. Press, W. H., B. P. Flannery, S. A. Teukolsky, and W. T. Vetterling. 1986. Numerical Recipes. Cambridge: Cambridge University Press.